357

Flow regimes of large-velocity-ratio coaxial jets

By H. REHAB, E. VILLERMAUX and E. J. HOPFINGER

LEGI/IMG - CNRS; UJF, INPG BP 53X, 38041 Grenoble Cedex, France

An investigation of the near-field flow structure of coaxial jets with large outer to inner velocity ratio r_u has been conducted. Since in all cases $r_u > 1$, the outer jet dominates the near-field flow structure. Two flow regimes are identified depending on whether r_u is larger or smaller than a critical value r_{uc}. When $r_u < r_{uc}$, the fast annular jet periodically pinches the central, slow jet near the end of the inner potential cone. The pinching frequency corresponds to the outer-jet mode. The length of the inner potential cone is strongly dependent on r_u and behaves like A/r_u, where A depends weakly on the initial conditions. When $r_u > r_{uc}$, the inner potential cone is truncated and is followed by an unsteady recirculation bubble with low-frequency oscillation.

The transition from one regime to another is explained by a simple model whose ingredients are the turbulent entrainment rate, governed by the outer-jet mixing layers and mass conservation. This model satisfactorily predicts the dependence of the inner potential cone length on r_u and the critical velocity ratio r_{uc}. The recirculation bubble has a wake-type instability. It oscillates at a low frequency and a large amplitude compared to the Kelvin–Helmholtz mode. Angular cross-correlations in the plane parallel to the jet outlet show moreover that this oscillation displays an azimuthal precession such that the rotation time of the phase of the oscillation equals the oscillation period. These salient features are discussed in the framework of the nonlinear delayed saturation (NLDS) model.

1. Introduction

Coaxial jets are a simple way by which two fluid streams can be mixed and this configuration is used for instance in combustion chambers of rocket engines. Often, one of the jets (the inner one) is in a liquid state and has to be atomized by a high-speed annular gas jet. This process, known as airblast atomization, has received considerable attention (Lefebvre 1989) during the past few decades. Most of the time the experiments have been aimed at characterizing the spray and have not allowed an analysis of the near-field flow structure and the instabilities in any detail. Leaving aside surface tension effects, the important parameters in this problem are the momentum flux ratio between the two streams $M = \rho_2 U_2^2 / \rho_1 U_1^2$ and the ratio of the outer to the inner nozzle diameters $\beta = D_2 / D_1$. When the fluid densities are the same, the momentum flux ratio reduces to the velocity ratio of the outer to inner jet $r_u = U_2 / U_1$. The near-field flow structure of coaxial jets in homogeneous fluids is, therefore, expected to be relevant to the understanding of liquid jet atomization. In the coaxial water jets studied here, quantitative flow visualizations can be used which are particularly helpful in the understanding of the interaction of different mixing layers present in the near field. This is well demonstrated by the laser-induced-fluorescence visualizations of coaxial water jets with $0.59 \leqslant r_u \leqslant 4.16$, performed by Dahm,
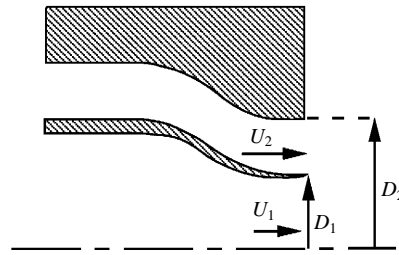
FIGURE 1. Coaxial jet nozzle configuration. D_1, D_2, U_1 and U_2 are the diameters and centreline exit velocities of the inner and annular jets respectively.

Clifford & Tryggvason (1992). These visualizations indicate clearly the importance of the parameter r_u.

Detailed measurements by Au & Ko (1987) of the mean velocity field of coaxial air jets with $1 \leqslant r_u \leqslant 6.6$ revealed the existence, in the near field, of three flow regions: an initial zone marked by the end of the outer potential cone whose length depends only slightly on r_u, an intermediate zone characterized by the inner potential cone whose length depends strongly on r_u and a third zone which starts at the reattachment point where the outer jet merges on the axis and pinches the inner one. The pinching of the inner jet by the large vortex structures of the outer mixing layer occurs at a frequency f similar to that of the convective instability of a single jet characterized by a Strouhal number $St_j = f D_2 / U_2 \approx 0.4$. Gladnick et al. (1990), using a CFC gas in the outer stream and air in the inner one and a velocity ratio of $r_u = 2$, observed a frequency peak corresponding to $St_j = 0.35$ on the concentration power spectra. This result shows the predominance of the faster stream in the structure of the flow.

The annular jet which is the limiting case of large-velocity-ratio coaxial jets ($r_u = \infty$) has been investigated in some detail. One of the first studies is by Miller & Comings (1960) where velocity, pressure and shear stress measurements have been made both in the near and far fields. Further experiments have been conducted by Chigier & Beer (1964), Ko & Chan (1978, 1979), Chan & Ko (1978). The flow structure in the wake region of an annular jet (Ko & Lam 1985; Lam & Ko 1986) is of particular interest.

The aim of the present paper is to clarify the different flow regimes in the near field of large-velocity-ratio coaxial jets $1 < r_u \leqslant \infty$. Two main flow regimes are identified, one when $1 < r_u < r_{uc}$ and the other when $r_{uc} \leqslant r_u \leqslant \infty$ where reverse flow is observed (Villermaux, Rehab & Hopfinger 1994). The value of r_{uc} lies between 5 and 8, depending on the velocity profiles at the nozzles. In §2 are presented the flow conditions and experimental procedures. The results concerning the regime $r_u < r_{uc}$ are discussed in §3 and the transition to the recirculation is explained in §3.5. The recirculating flow bubble which exists when $r_u \geqslant r_{uc}$ is discussed in §4. Its pulsating mode is depicted and explained in §4.3 in the framework of a time-delay model (the NLDS model, see Villermaux 1994; Villermaux & Hopfinger 1994a,b).

2. Flow conditions and procedures

The experimental set-up consists of coaxial axisymmetric water jets discharging into a tank where the fluid (water) is at rest. The nozzle configuration used is shown in figure 1. The convergent nozzles (figure 1) have inner and outer diameters of $D_1 = 2$ cm and $D_2 = 2.7$ cm and contraction ratios of 2 and 4 respectively. The area ratio at the nozzle exit is 1.82.
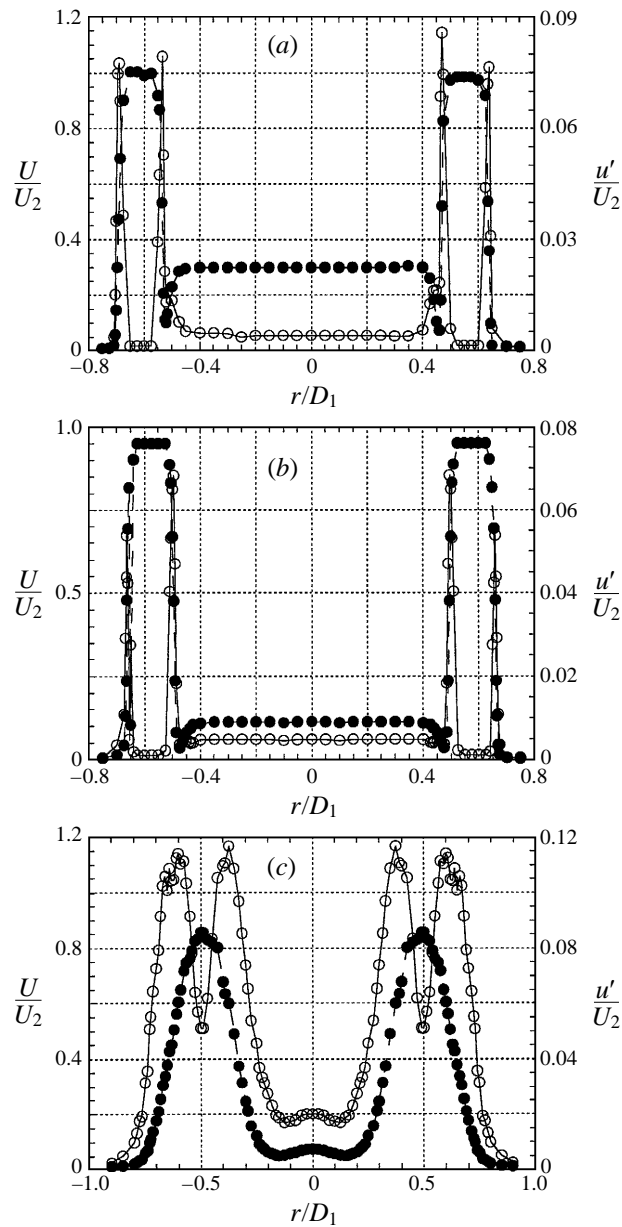
FIGURE 2. Radial profiles of mean axial velocity ($\bullet$), and r.m.s. values of velocity fluctuations ($\circ$): (a) $r_u = 3$ at $x = 2\,\text{mm}$; (b) $r_u = 10$ at $x = 2\,\text{mm}$ and (c) $r_u = 10$ at $x/D_1 \approx 1$.

The exit velocities in our investigations covered the ranges $0 \leqslant U_1 \leqslant 1\,\text{m s}^{-1}$ and $0.3 \leqslant U_2 \leqslant 4\,\text{m s}^{-1}$. The Reynolds number defined from momentum conservation, $Re = (U_2 D_2/v)[1 - (D_1/D_2)^2]^{1/2}$, when $r_u \gg 1$ ranges from 10^4 to 10^5. Mean and turbulent velocity measurements were made with a constant-temperature hot-film anemometer. The cylindrical probe used has $0.5\,\text{mm}$ active length and $25\,\mu\text{m}$ diameter (aspect ratio of 20), operating at an overheat ratio of 5%. Only the axial velocity component U in the principal direction of the flow was measured.

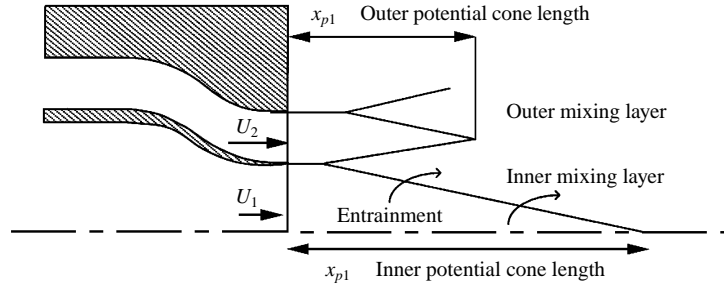In figure 2, the radial profiles of the mean velocity and the root-mean-square

FIGURE 3. Schematic diagram of the mixing layers in the near field.

(r.m.s.) value of velocity fluctuations at the nozzle exit ($x \approx 2$ mm downstream) are presented (for the convergent nozzle jets) for $r_u = 3$ and $r_u = 10$ ($U_2 = 2 \, \mathrm{m \, s^{-1}}$). For $U_2 = 2 \, \mathrm{m \, s^{-1}}$ the Reynolds number defined with the initial boundary layer thickness δ_0, $Re_{\delta_0} = U_2 \delta_0 / v$, is about 800. The maximum r.m.s. value of the velocity fluctuations in the boundary layers is of the order of $0.08 U_2$. The fluctuation level in the central jet is $0.01 U_2$ and is nearly zero in the annular jet. This is attributed to the stronger contraction of the annular nozzle. Further downstream, mixing layers develop (figure 2c) and the velocity fluctuations reach $0.12 U_2$ at $x/D_1 = 1$ for $r_u = 10$.

Mean static pressure measurements, with respect to the local hydrostatic pressure, have been made with a pressure probe linked to an HMB-KWS differential pressure sensor. The pressure tube, of Pitot tube design, 3 mm outer diameter, is placed parallel to the flow direction to prevent flow perturbations. The mean static pressure measurements are affected by the turbulent fluctuations and what we actually measure is:

$$P = P_{st} + \tfrac{1}{2} \rho u'^2.$$

In the regions where velocity fluctuations are important, the turbulent dynamic pressure $\tfrac{1}{2} \rho u'^2$ is of the order of P_{st}.

The visualizations have been realized by a laser-induced-fluorescence technique, using disodium fluorescein dye as a passive tracer, excited by an argon-ion laser sheet. Both the central and the annular streams can be seeded with dye by means of injection into mixing chambers upstream of the nozzles. The fluorescein concentrations used during the experiments were of the order of $10^{-7} \, \mathrm{m \, l^{-1}}$ at the nozzle exit. A thin and uniform laser sheet (0.5 mm thick) was produced along the jet axis by reflection of a laser beam on a mirror oscillating at 4 kHz. The images were taken by a CCD camera at a rate of 50 frames per second and with an exposure time $1/1000$ second. The images were then digitized on 256 grey levels and 512×768 pixels. The pixel resolution corresponds to a real dimension of 0.3 mm.

3. The flow structure and potential cone length for $r_u \geqslant r_{uc}$

3.1. *Flow visualization*

The near-field flow structure of turbulent coaxial jets ($x/D_1 \approx 5$) is characterized by the development of two axisymmetric free turbulent mixing layers (figure 3). The growth of the inner shear layer between the central and annular streams depends on r_u while the external layer between the outer jet and the ambient fluid at rest grows independently of the velocity ratio r_u. Figure 4 shows instantaneous pictures of the near-field flow structure with the annular jet seeded with fluorescent dye. The laser
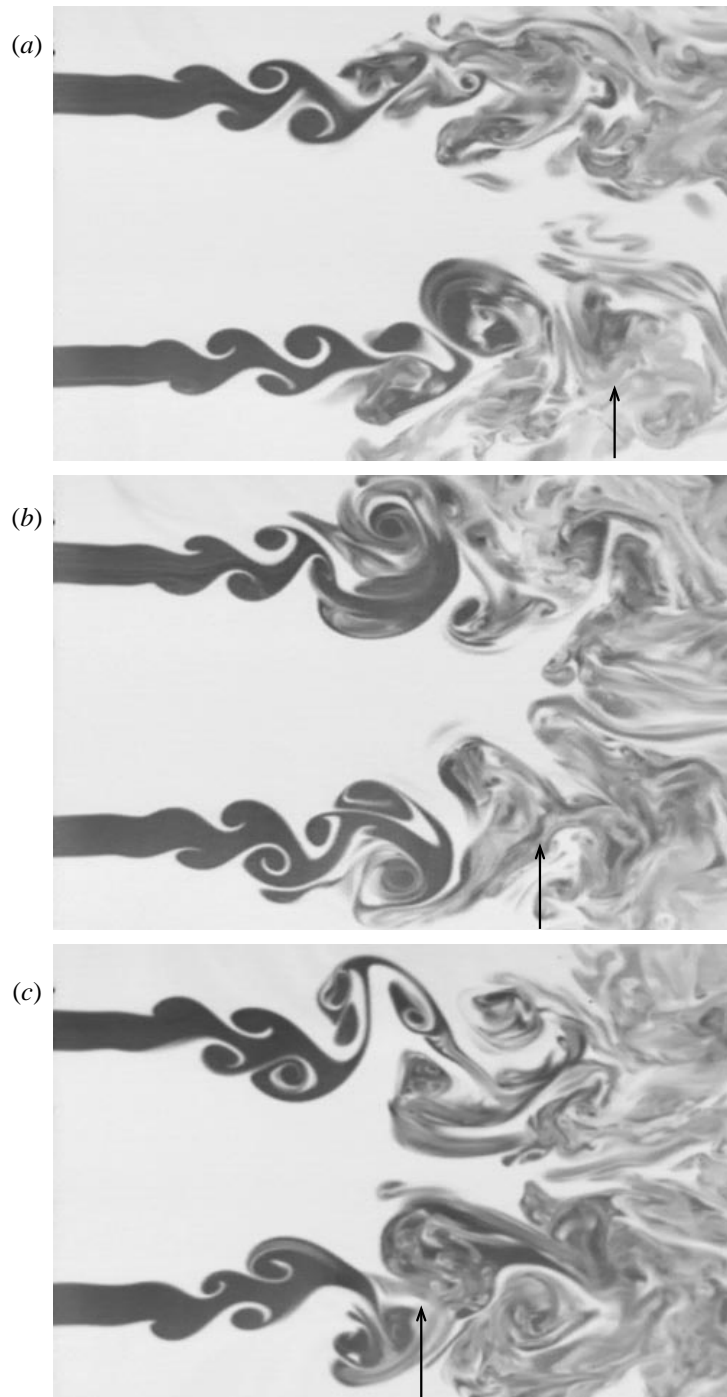
FIGURE 4. Instantaneous pictures of the flow structure for (*a*) $r_u = 2$; (*b*) $r_u = 3$; (*c*) $r_u = 4$. The annular jet (dark) is seeded with fluorescent dye and the laser light sheet cuts through the central plane. The arrow indicates the pinching location. View from $x = 0$ to $x/D_1 = 3$.
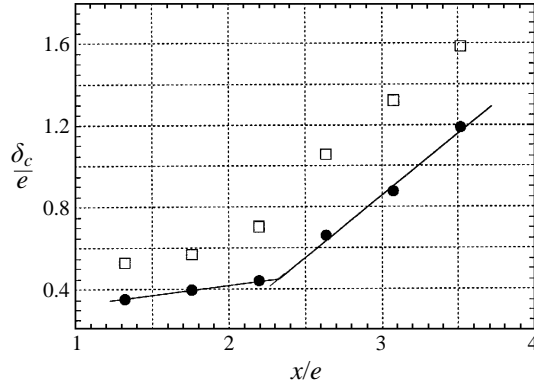
FIGURE 5. Inner mixing layer concentration thickness variations versus x/e with $U_1 =$ constant. ●, $U_2 = 0.4$ m s^{-1}; □, $U_2 = 0.8$ m s^{-1}. $e = \frac{1}{2}(D_2 - D_1)$.

light sheet is parallel to the jet axis and cuts through the centreplane. The velocity U_2 is unchanged, while U_1 is decreased from figure 4(a) to 4(c). The Reynolds number Re as defined in §2 is of the order of 7000. For the three velocity ratios considered, $r_u = 2, 3$ and 4, which correspond to figure 4(a), 4(b) and 4(c) respectively, the fast outer jet dominates the dynamics. It is observed that the structures of the outer mixing layer pinch the central jet at the end of the inner potential cone. It is also clear that the inner potential cone length decreases when r_u is increased. The two mixing layers develop initially independently of each other, then, downstream of $x/D_1 \approx 1$, which corresponds approximately the outer potential cone length, the outer-layer structures interact with those of the inner layer in a way reported by Dahm *et al.* (1992). Furthermore, the mixing layer instability develops at a certain distance x downstream of the nozzle exit, with x depending on both U_1 and U_2. If U_1 is maintained constant, the evolution of this distance with U_2 is measured on dye concentration images averaged over 200 instantaneous images.The mixing layer instability starting point x for a certain value of U_2 is indicated by the change in the spatial growth of the concentration thickness δ_c defined by $\delta_c = C_0/(dC/dy)_{max}$, where C_0 is the mean maximum concentration at the nozzle exit and y the normal direction. Figure 5 shows the evolution of δ_c as a function of x for $U_2 = 0.4$ m s^{-1} and $U_2 = 0.8$ m s^{-1}. It appears that δ_c grows linearly with x with two different rates. First, the rate of increase of δ_c is weak and due principally to molecular diffusion. Then, it strongly increases due to the development of the shear layer instability. The location of the onset of instability is determined from the intersection of these two lines of growth. We obtain $x/2e = C Re_g^{-1/2}$, where $e = \frac{1}{2}(D_2 - D_1)$ and $Re_g = U_2 2e/v$, with $C = 78$ and 110 for the inner and the outer layers respectively. This is in good agreement with Becker & Massaro (1968) for a single round jet.

3.2. *Potential cones and characteristic frequencies*

The length of the inner 'potential' cone (potential here need not mean irotational but designates a region of weak turbulent intensity where small-scale dissipation is nearly zero (Landau & Lifchitz 1989)) strongly depends on the velocity ratio r_u and decreases as r_u increases. The average shape of the inner cone, obtained by averaging over 500 instantaneous images, is illustrated in figure 6. The outer potential cone, whose length is only weakly dependent on r_u, delimits the region where U_2 is approximately constant. Its length x_{p2} (figure 3), is essentially fixed by the diameter
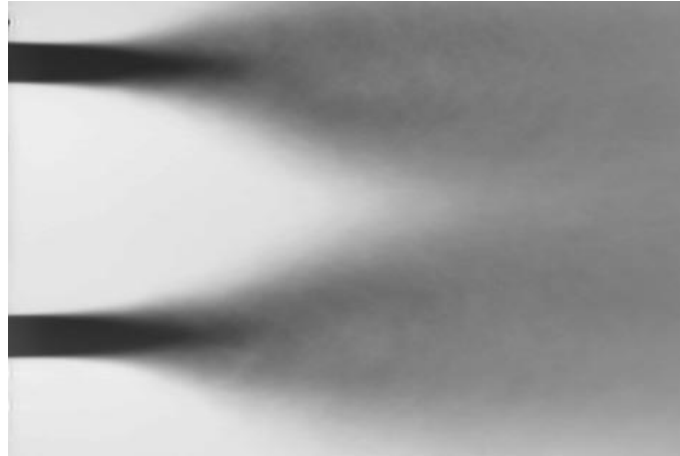
FIGURE 6. Image of mean concentration field for $r_u = 4$, $Re \approx 7200$. The annular jet (dark) is seeded.
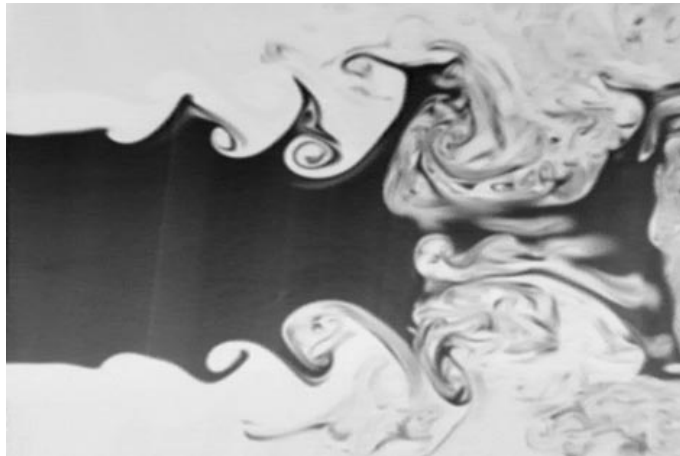

FIGURE 7. Visualization of the inner potential cone for $r_u = 3$. The fluorescent dye is here injected in the inner jet (dark).

ratio β. For the present geometry of $\beta = 1.35$, $x_{p2} \approx 2\,\text{cm} = D_1$. Beyond this distance the outer mixing layer interferes with the inner one and penetrates rapidly toward the centre (figures 4 and 7). The penetration, accompanied by a pinch-off of the inner cone, occurs periodically at a frequency f corresponding to the fundamental mode of Kelvin–Helmholtz instability. The Strouhal number $St_j = fD_2/U_2$, where f is defined by the frequency peak of the velocity fluctuation spectrum measured at the end of the inner potential cone, is close to 0.27, with U_2 in the range $0.3 < U_2 < 3\,\text{m\,s}^{-1}$. This value of the Strouhal number corresponds to the value commonly agreed for single jets (Crow & Champagne 1971; Ho & Huerre 1984).

The inner mixing layer convective instability starts close to the jet exit, and corresponds to higher frequencies ($f \approx 500\,\text{Hz}$). Based on the initial momentum thickness θ_0 (θ_0 is calculated by integration of the mean velocity exit profile shown in figure 2*a*), and the convection velocity $U_c = \frac{1}{2}(U_1 + U_2)$, the Strouhal number $St_\theta = f\theta_0/U_c$ is approximately 0.034 in agreement with the expected value (Ho & Huerre 1984).
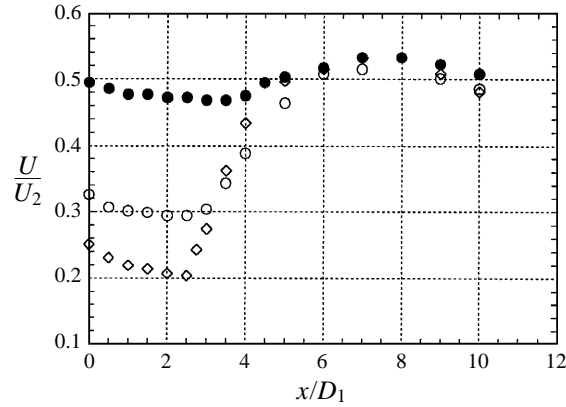
FIGURE 8. Axial mean velocity variations along the jet axis. $\bullet$, $r_u = 2$; $\circ$, $r_u = 3$; $\diamond$, $r_u = 4$.
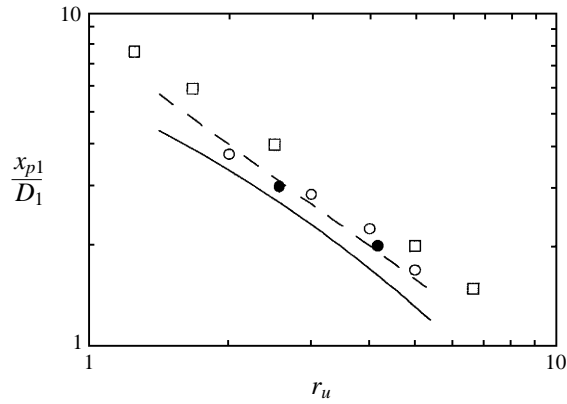

FIGURE 9. Dependence of the inner potential cone length on velocity ratio for $\beta = 1.35$: $\circ$, determined from velocity variation; - - -, $8/r_u$; —, present model solution; $\square$, $\beta = 2$ (Au & Ko 1987); $\bullet$, $\beta = 1.4$ (Dahm *et al.* 1992 estimated from their images, figures 10 and 11).

When $x/D_1 > 1$, this frequency disappears and the dynamics is dominated by the outer mixing layer.

3.3. *Velocity field and pressure distributions*

It is seen from figure 8 that for a given velocity ratio in the range $1 < r_u < 8$, the mean velocity at the jet axis decreases with downstream distance and reaches a minimum near the end of the inner potential cone where the annular, outer mixing layer impinges on the axis. From there on the flow accelerates until about $x/D_1 \approx 7$. Beyond this position, the mean velocity starts to decrease in the same way as in a single axisymmetric jet. In figure 8 are presented the mean velocity variations along the axis for the three values of $r_u = 2, 3$, and 4 with the outer velocity fixed to $2 \, \text{m s}^{-1}$. The longitudinal position where the minimum is reached corresponds to the potential cone length x_{p1}. Based on this criterion, and as a function of velocity ratio r_u (figure 9), x_{p1} can be represented by the relation

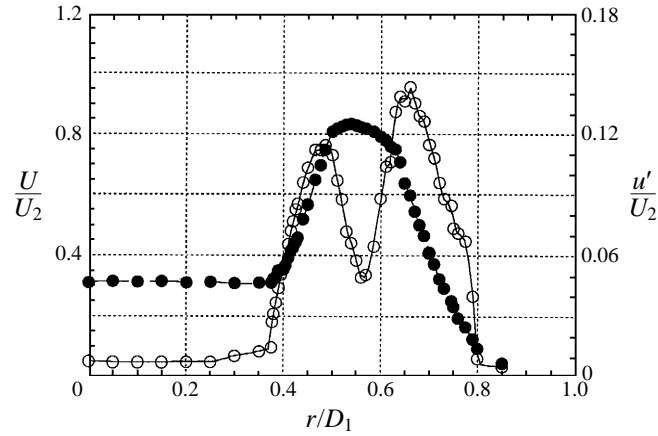$$\frac{x_{p1}}{D_1} \approx \frac{8}{r_u},$$

FIGURE 10. Mean velocity profile and r.m.s. values of velocity fluctuations for $r_u = 3$ measured at $x/D_1 = 1$. The turbulent intensity in the inner mixing layer is $u' = 0.12U_2 = 0.17(U_2 - U_1)$, $U_2 = 2$ m s^{-1}.

where the numerator is specific to the present geometry. Also included in figure 9 are the results of Dahm *et al.* (1992) and Au & Ko (1987). Au & Ko used a diameter ratio of $\beta = 2$ and $1.25 \leqslant r_u \leqslant 6.6$. Their results can be correlated by $x_{p1}/D_1 \approx 9.9/r_u$. The result of Au & Ko is quite logical because for a given r_u, when β increases, the annular gap is larger, hence the outer potential cone is longer, so that the pinching of the inner jet occurs further downstream. Dahm *et al.* have noticed that for a given r_u, when the jet velocities are increased, the inner potential cone length is slightly shorter. The main reason for this is that the outer mixing layer develops earlier when the Reynolds number is larger. This Reynolds number effect is however weak compared with the velocity ratio effect.

The drop in velocity within the central potential cone is due to the entrainment of inner fluid into the annular mixing layers. The large vortex structures that develop within the mixing layers are principally responsible for this entrainment (Liepmann & Gharib 1992). These incorporate fluid at a rate proportional to the local turbulent intensity in the mixing layer $u' = \alpha(U_2 - U_1)$ with $\alpha \approx 0.17$ (see figure 10 and Browand & Latigo 1979; Hussain & Zedan 1978; Brown & Roshko 1974). The pressure drop associated with the entrainment by the mixing layer is thus expected to be of the order of (Villermaux *et al.* 1994)

$$\Delta P = \tfrac{1}{2}\rho u'^2$$

or

$$\frac{\Delta P}{\tfrac{1}{2}\rho U_2^2} = \alpha^2 \left[1 - \left(\frac{1}{r_u} \right) \right]^2.$$

In figure 11, the radial variation of the measured mean static pressure $P = P_{st} + \tfrac{1}{2}\rho u'^2$ and P_{st} at $x/D_1 \approx 0.75$ are shown for $r_u = 4$. It is seen that when P is corrected by subtraction of the dynamic turbulent pressure term $(\tfrac{1}{2}\rho u'^2)$ the pressure drop, established by the inner mixing layer, is in good agreement with the expected value $(\Delta P/(\tfrac{1}{2}\rho U_2^2) \approx 0.02)$.

3.4. *Entrainment model*

The aim of this model is to predict the inner potential cone length for $1 < r_u < 8$. The formulation that we adopt here is very similar to that of Villermaux & Durox (1992)
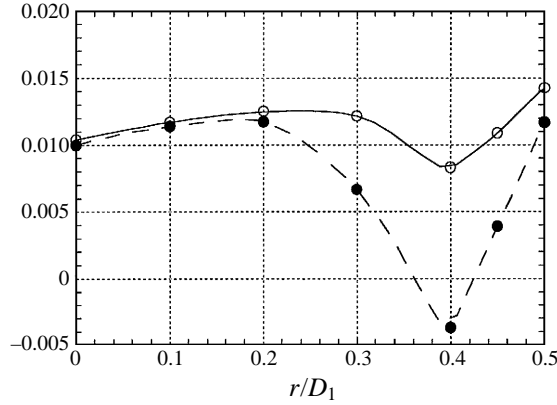
FIGURE 11. Mean radial static pressure profile at $x/D_1 = 0.75$, $r_u = 4$.
$\circ$, $P/(\frac{1}{2}\rho U_2^2) = (P_{st} + \frac{1}{2}\rho u'^2)/(\frac{1}{2}\rho U_2^2)$; $\bullet$, $P_{st}/(\frac{1}{2}\rho U_2^2)$.

in the context of laminar jet diffusion flames, and Villermaux (1995a) concerning the shape and extent of reaction–diffusion interfaces in turbulent media. The basic idea consists in assuming that the global flow rate of the entrained fluid (here the inner flow), has to cross the interface through which entrainment takes place. A mass balance involving the total surface of entrainment and a suitable expression for the entrainment velocity provide a closure equation from which one derives the (mean) surface of entrainment, and thus its length. The mass conservation equation for an incompressible fluid can be written as

$$\tfrac{1}{4}\pi D_1^2 \overline{U_1} = \tfrac{1}{2}\pi D_1 \left[\left(\tfrac{1}{2}D_1\right)^2 + x_{p1}^2 \right]^{1/2} u_e, \tag{1}$$

where $\overline{U_1}$ is the inner jet bulk velocity and u_e an entrainment velocity of inner jet fluid into the mixing layer. This means that all the fluid injected through the inner nozzle (the term on the left-hand side) is entirely entrained across the surface of the inner cone of base D_1 and height x_{p1}, with an entrainment velocity u_e (the term on the right-hand side). In equation (1), the volume pinched off at the end of the inner potential cone is neglected. This leads to an overestimation of the entrained fluid through the cone surface.

The entrainment velocity is expressed in terms of the turbulent intensity by the following entrainment hypothesis:

$$u_e = Cu', \tag{2}$$

where the constant $C \approx 0.5$ is determined from the mass conservation for a single jet, knowing that its cone length is approximatly $6D_0$ (Hinze 1959); D_0 is the jet diameter. $u' \approx 0.17(U_2 - U_1)$ is the turbulent intensity within the mixing layer (figure 10).

Let us first consider the case where $x_{p2} \ll x_{p1}$ (small annular gap). The velocity scale that fixes u' at the entrainment interface is then U_2 rather than ΔU because the annular jet actually dominates rapidly the inner stream and imposes the entrainment law by a velocity $(U_2 - U_1) < U < U_2$. For simplicity we take $U = U_2$, that is to say $u' = \alpha U_2$. The expression for the entrainment velocity is then $u_e = C\alpha U_2$.

Thus, equation (1) gives

$$\frac{x_{p1}}{D_1} \approx \frac{1}{2} \left(\frac{1}{C^2 \alpha^2 r_u^2} - 1 \right)^{1/2} \approx \frac{1}{2C\alpha r_u};$$

or, with $\alpha = 0.17$,

$$\frac{x_{p1}}{D_1} \approx \frac{6}{r_u}. \tag{3}$$

The important point to note is that the velocity ratio r_u emerges as the most significant parameter and in the form of a power law (Villermaux *et al.* 1994)†.

When the annular gap is large the inner and the outer potential cone lengths are of the same order $x_{p2} \approx x_{p1}$. In this case the turbulent intensity is fixed by the velocity difference $(U_2 - U_1)$ that is $u' = \alpha(U_2 - U_1)$. The entrainment velocity is then given by

$$u_e = C\alpha(U_2 - U_1)$$

and consequently, with $\alpha = 0.17$

$$\frac{x_{p1}}{D_1} \approx \frac{1}{2} \left(\frac{1}{C^2\alpha^2(r_u - 1)^2} - 1 \right)^{1/2}. \tag{4}$$

For a given velocity ratio r_u, the inner potential cone length given by (4) is longer than in the previous case (3) because the entrainment rate, averaged over the whole cone length, is weaker. This explains the effect of D_2/D_1 on x_{p1}.

A more general formulation of the model is to consider two regions with the corresponding entrainment velocities. The expression obtained is

$$\overline{U}_1 = C\alpha[U_2 + U_1(Y^2 - 1)] \left[1 + \left(\frac{2x_{p2}/D_1}{1 - Y} \right)^2 \right]^{1/2}, \tag{5}$$

where $Y = 1 - x_{p2}/x_{p1}$. Equation (5) is an implicit equation of order six in x_{p1}, and has to be solved numerically. The ratio of the maximum to the bulk velocities for the present geometry is close to 1 (flat mean velocity profiles at the nozzles). The solution of (5) is illustrated on figure 9 and compared with the relation $8/r_u$ and the experimental data. It is clear that the theoretical and experimental points are in a good agreement even though the model underestimates somewhat the cone length. A simple $8/r_u$ law is a good approximation for the dependency of the inner cone length on the velocity ratio r_u. To sum up this section, we emphasize the predictive character of the model which seems to contain the correct physics of the near-field flow. We should emphasize that the regime described here concerns values of r_u in the range $1 < r_u < 8$ because beyond this range a recirculating flow regime is established, as discussed below.

The geometry of the coaxial injectors and the initial flow conditions (tube jets for example) do not alter the central potential cone variation law with r_u i.e. $x_{p1}/D_1 = A/r_u$, but act on the value of the numerical constant A which lies between 5 and 9 (Rehab, Villermaux & Hopfinger 1997).

3.5. *Transition to a recirculation regime*

If the velocity ratio is increased to $r_u = r_{uc}$ and beyond, it is observed that the outer-jet fluid begins to penetrate upstream on the inner jet axis. For $r_u = 6$ (figure 12*a*) there is no reverse flow in the mean, whereas for $r_u = 8$, figure 12(*b*), there is weak mean reverse flow and the inner potential cone is truncated. The case of $r_u = 15$ (figure 12*c*)

† When the fluid densities are not the same, it is easily demonstrated using Hill's (1972) results that $u_e \approx K\left(\rho_1/\rho_2\right)^{-1/2} u'$ and r_u is then replaced by $M^{1/2}$ in equations (3) and (4), where $M = \rho_2 U_2^2 / \rho_1 U_1^2$.
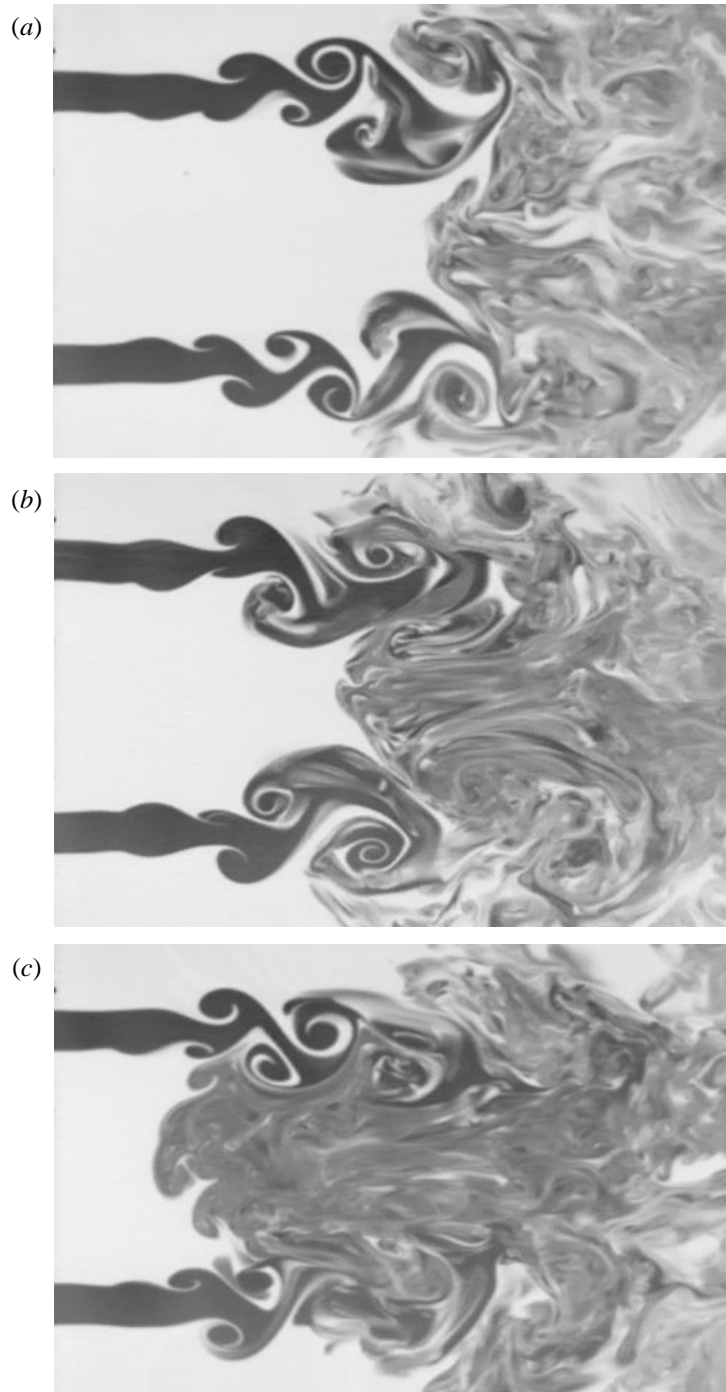
(*a*)

(*b*)

(*c*)

Figure 12. Instantaneous pictures of the flow structure as in figure 4 but for
(*a*) $r_u = 6$; (*b*) $r_u = 8$; (*c*) $r_u = 15$.

is characterized by a recirculating flow cavity in which the reverse flow nearly reaches the jet nozzle and the dynamics is entirely governed by the outer stream (Villermaux *et al.* 1994). The aim in this section is to understand how and why the transition to the recirculating regime occurs. We have already stated that for $r_u = 4$ and in general in the regime without a cavity flow, the entrainment process by the outer jet is linked to a radial pressure jump

$$\Delta P = \tfrac{1}{2}\rho u'^2,$$

where $u' = \alpha(U_2 - U_1)$. As long as the inner incident kinetic pressure $\tfrac{1}{2}\rho \overline{U_1}^2$ is larger than ΔP, the inner jet is able to prevent the formation of a recirculating flow. When r_u is increased beyond a certain value, ΔP may exceed $\tfrac{1}{2}\rho \overline{U_1}^2$ and reverse flow is possible. This new flow regime, characterized by a central recirculating cavity, occurs at a critical velocity ratio r_{uc} which represents the recirculation threshold. The recirculation commences when

$$\tfrac{1}{2}\alpha^2 \rho (U_2 - U_1)^2 = \tfrac{1}{2}\rho \overline{U_1}^2$$

giving

$$r_{uc} = \left[\frac{1}{\alpha U_1/\overline{U_1}} + 1 \right] \approx 7; \quad \alpha = 0.17.$$

It is found experimentally that the critical value of r_{uc} is close to 8 (§4.1). This is an average value where recirculation is just about observable. In other words the length of the potential cone oscillates about a mean value.

Along the x-axis, two forces are acting with opposing effects to realize a force–momentum balance in the near field. The first one is the axial mean static adverse pressure gradient which tends to decelerate the flow and causes backflow towards the inner jet nozzle. The second one is the radial turbulent shear stress gradient which accelerates the flow in the positive x-direction against the static pressure gradient (Miller & Comings 1979; Champagne & Wygnanski 1971). At the threshold of the recirculation the mean central velocity of backflow is zero and the turbulent stress gradient effect compensates for the static pressure gradient. To clarify these trends, mean static pressure and mean velocity measurements along the axis have been made. In figure 13 is presented the distribution of the mean static pressure P along the central axis for $r_u = 8$. This evolution shows a low-pressure zone extending from the exit of the inner jet until about $x \approx D_1$ downstream where P reaches a local minimum of -0.03 ($\tfrac{1}{2}\rho U_2^2$) corresponding to maximum reverse flow. Beyond $x \approx D_1$, the mean static pressure increases markedly and has a positive peak of $+0.09$ ($\tfrac{1}{2}\rho U_2^2$) at $x/D_1 \approx 1.5$. This maximum is the location of the downstream end of the recirculation cavity where the mean velocity is nearly zero (stagnation point). This axial pressure gradient is responsible for the onset of the reverse flow.

In figure 13 the axial variation of static pressure for $r_u = 4$ is also shown for comparison. There is a significant change when r_u is increased from 4 to 8 showing a considerable increase in pressure difference. For instance, the axial distribution of static pressure for $r_u = 4$ shows that the kinetic pressure $\tfrac{1}{2}\rho U_1^2$ is strong enough to accelerate the flow in the positive direction, preventing reverse flow. As r_u approaches r_{uc} there is increased entrainment and a reduction of the exchange surface so that $\tfrac{1}{2}\rho U_1^2$ is no longer sufficient to prevent reverse flow.
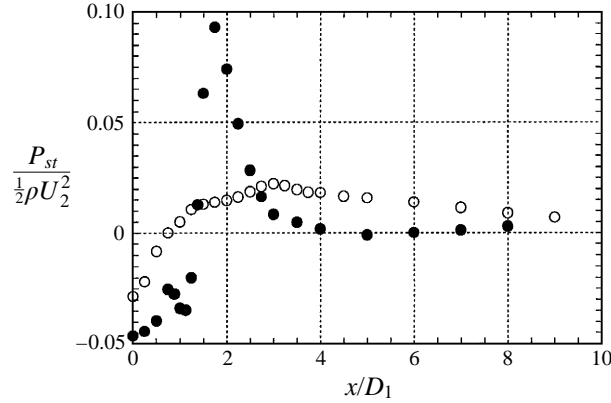
FIGURE 13. Mean static pressure distribution along the axis: $\bullet$, $r_u = 8$; $\circ$, $r_u = 4$.

4. Features of the recirculating flow bubble

When $r_u \geqslant r_{uc}$, the near-field flow pattern is characterized by the formation of a recirculating flow cavity of wake-type structure. The size of the cavity is zero for $r_u = r_{uc}$ which represents a point on the axis of maximum pressure (stagnation point). As r_u increases, the length of the recirculating zone also increases and reaches a length approximately equal to D_1 when $r_u = \infty$ ($U_1 = 0$). In general, the recirculating cavity is limited by two stagnation points. The upstream one and the downstream point of maximum static pressure which is the location of the closure of the cavity. This axial pressure gradient maintains the reverse flow so that the mean reverse flow velocity is more and more important as r_u increases. The near-field flow structure thus consists of a truncated cone of base D_1 with turbulent entrainment by the faster stream on its boundaries. Notice that beyond the stagnation point x_{s2} ($x/D_1 = 1.75$) (figure 13) the static pressure decreases rapidly so that any packet of fluid which is just downstream of x_{s2} is immediately entrained towards the far field. This zone, downstream of x_{s2}, corresponds to the merging of the inner and the outer mixing layers on the axis. This merging is accompanied by an oscillation in pressure amplitude corresponding to the passage frequency of the dominant vortex structures of the outer mixing layer. The frequency, of Strouhal number $St = f D_2/U_2 = 0.35$, is characteristic of the preferred jet mode.

4.1. *Velocity and pressure field*

In this section, we characterize the mean and fluctuation velocity fields along the axis for $r_u \geqslant r_{uc}$. Figures 14 and 15 illustrate the evolution of mean and r.m.s. velocities for $r_u = 8, 9$ and ∞ for a fixed outer velocity ($U_2 = 2\,\mathrm{m\,s}^{-1}$, $Re = 3.6 \times 10^4$). The mean velocity distributions show a velocity peak representing the maximum reverse flow intensity (this peak is in fact negative but the single hot film is not able to distinguish between negative and positive velocities). This peak indicates the existence of a backflow. It is seen that both the intensity of the mean flow and the turbulent intensity, and consequently the mixing of the two streams, increase with r_u. Figure 14 reveals that for $r_u = 8$, the recirculation is very weak. However, when $r_u = 9$ a noticeable mean velocity peak U_R of $0.08U_2$ at $x \approx 1.25D_1$ shows the existence of reverse flow. We thus estimate that $r_{uc} \approx 8$. Increasing r_u to ∞ the recirculation is clearly more intense with $U_R \approx 0.3U_2$. The location in the peak of the mean flow which moves towards the exit of the jets when r_u is increased. Its minimum for $r_u = \infty$
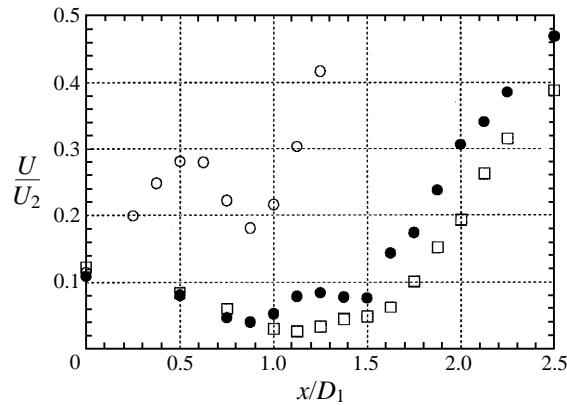
FIGURE 14. Axial mean velocity variations along the jet axis: $\square$, $r_u = 8$; $\bullet$, $r_u = 9$; $\circ$, $r_u = \infty$.
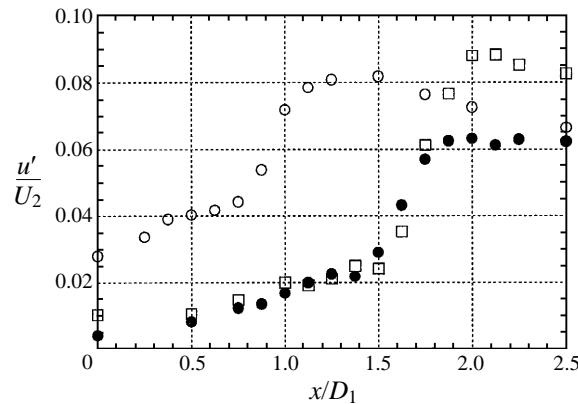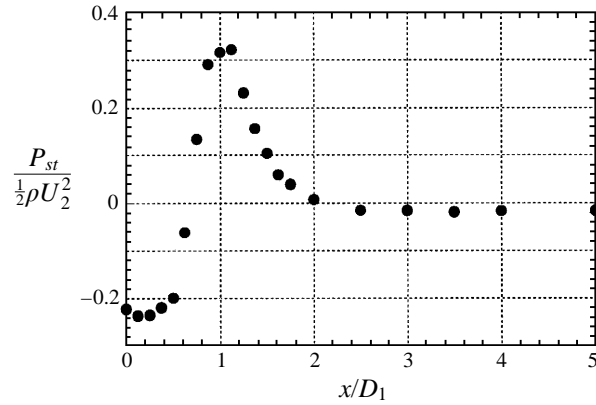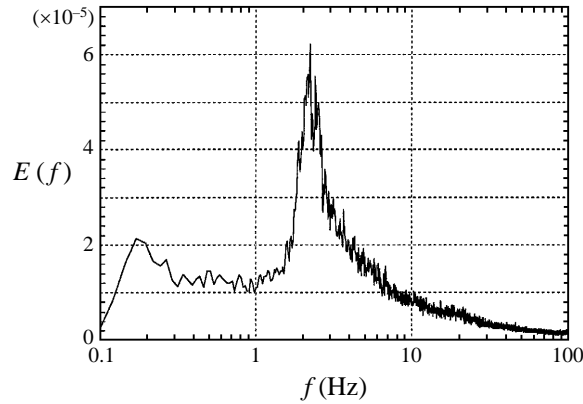

FIGURE 15. Turbulent velocity fluctuations variations along the jet axis:
$\square$, $r_u = 8$; $\bullet$, $r_u = 9$; $\circ$, $r_u = \infty$.

is located at $x/D_1 = 0.5$. Furthermore, the location of the maximum of the mean flow corresponds to a concentration of turbulent intensities of $0.04U_2$ at the centre of the cavity. The turbulent fluctuations reach about $0.08U_2$ at the downstream end of the bubble (figure 15).

We determine the size of the recirculation bubble from the locations of the two minima in mean velocity which correspond to the upstream (x_{s1}) and downstream (x_{s2}) stagnation points delimiting the backflow zone. These positions have an unsteady oscillatory motion so that x_{s1} and x_{s2} represent mean quantities. The length of the cavity given by $x_{s2} - x_{s1}$ has a strong dependence on r_u with a maximum for $r_u = \infty$ ($x_{s2} - x_{s1} \approx D_1$).

The pure annular jet ($r_u = \infty$) has been the subject of a large number of investigations. The measured maximum of the mean reverse flow velocity which is a constant fraction of U_2 ($0.3U_2$) is in good agreement with the results of Ko & Chan (1979) who found a constant (normalized by $\frac{1}{2}\rho U_2^2$) mean static pressure gradient on the axis between the centre of the bubble and the downstream stagnation point x_{s2}. The axial mean static pressure distribution P, shown in figure 16, reaches a maximum of $0.3(\frac{1}{2}\rho U_2^2)$. For comparison recall that for $r_u = 8 \approx r_{uc}$, the same jump was only about

FIGURE 16. Mean static pressure variation along the axis, $r_u = \infty$.

FIGURE 17. Velocity fluctuation spectrum measured on the axis at $x/D_1 \approx 1$, $r_u = \infty$.

$0.13(\frac{1}{2}\rho U_2^2)$ (figure 13). However, the turbulence intensity (normalized by U_2) depends on U_2 and is more important when U_2 is larger.

4.2. *Bubble oscillation*

An important aspect of the recirculation flow problem is the type of instability it develops and its dependence on the dynamic and geometric parameters of the system. A wake-type mode was first detected for $r_u \approx 10$, leading to $U_R/U_2 \approx 0.15$, a value of the same order as found by Strykowski & Niccum (1991). The recirculating bubble is unsteady and oscillates periodically with a characteristic frequency distinct from the Kelvin–Helmholtz instability mode. The oscillation frequency and amplitude shown in figure 17 have been measured at the downstream end of the bubble ($x \approx D_1$) for $r_u = \infty$ where the oscillatory movements are strongest. The corresponding Strouhal number of the bubble pulsation based on D_1 (characteristic size of the recirculating cavity) and on U_2 (characteristic velocity of the backflow regime) (figure 18) is, in our geometry, $St_b = fD_1/U_2 \approx 0.035$, which is an order of magnitude lower than the Strouhal number associated with the Kelvin–Helmholtz mode. Further downstream ($x/D_1 \approx 2$), the amplitude of the pulsation decreases (figure 19) and at $x/D_1 \approx 3$, only the preferred jet mode persists.
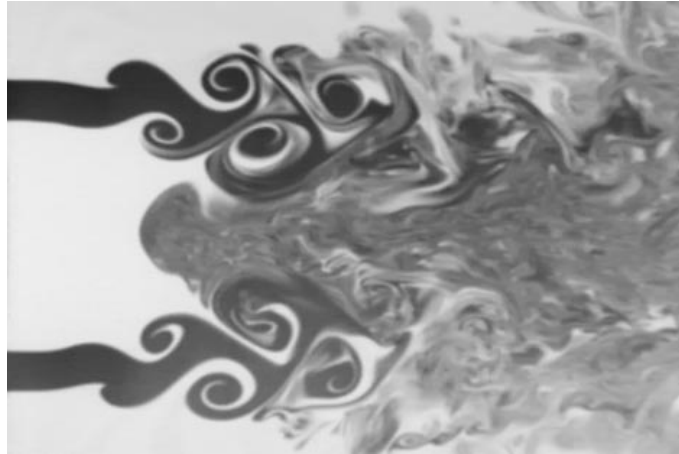
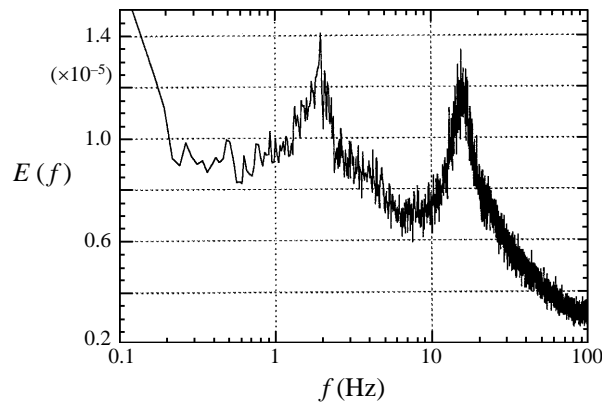FIGURE 18. Instantaneous picture as in figure 4, but for $r_u \gtrsim 8$.

FIGURE 19. Velocity fluctuations spectrum measured at the boundary of the recirculation bubble measured at $x/D_1 \approx 2$, $r_u = \infty$.

The oscillatory mode of the recirculation cavity is, in fact, an azimuthal mode. This mode consists of a deformation of the bubble around its mean shape (figure 20), so that the oscillation observed on a point at its boundary corresponds to the passage of the deformation of the bubble past the probe during its rotation. In figure 20, cases (*a*), (*b*) and (*c*) describe a half-period of bubble rotation. In order to characterize this precession mode, velocity cross-correlations in the azimuthal plane measurements were made for $r_u = \infty$. The experimental procedure consists of using two hot-film velocity probes with the first one, $S1$, fixed at the boundary of the bubble and the other, $S2$, moved at the same x-location in the azimuthal direction relatively to $S1$. The velocity cross-correlations measured for phase angle $\phi = 270°$ between the two probes is shown in figure 21. From all the measurements it is observed that the time shift τ_s of maximum correlation varies linearly with ϕ (figure 22). For instance, when $\phi = 180°$, the two probes are symmetrically opposite and the time shift τ_s is approximately half the oscillation period of the recirculation cavity. The pulsation mode is a pure precession mode ($m = 1$) similar to the one observed by Berger, Scholz & Schumm (1990) in the wake behind a sphere. In other words the
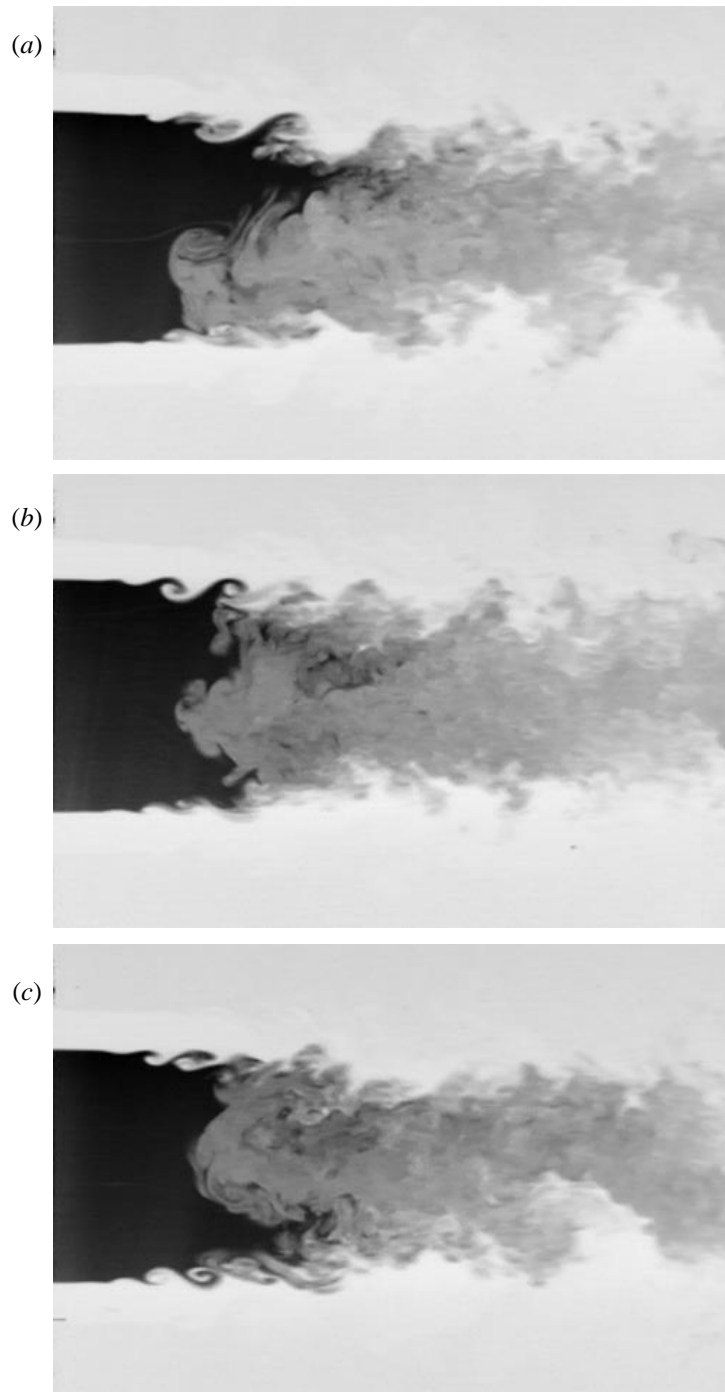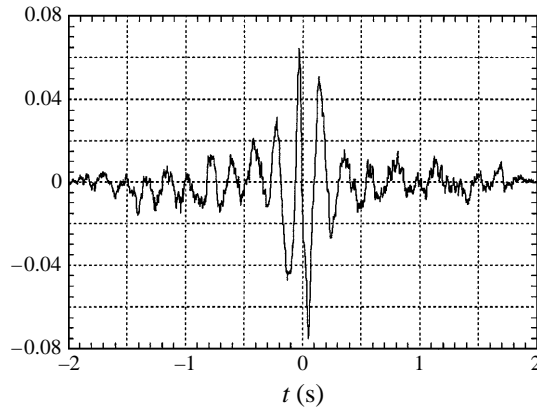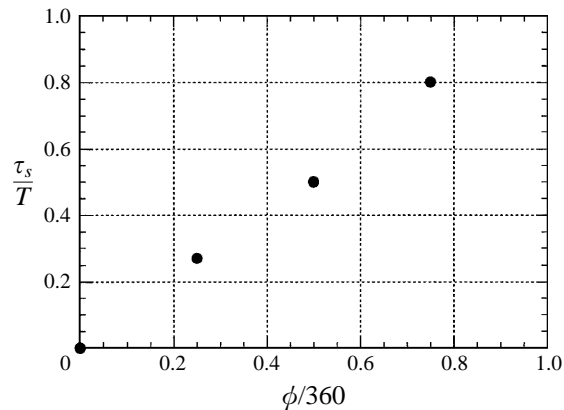
FIGURE 20. Instantaneous pictures showing half a period of rotation of the recirculation bubble at $r_u \approx 15$ and (a) t (b) $t + \frac{1}{4}T$, (c) $t + \frac{1}{2}T$; T is the rotation period. Fluorescent dye is injected in the central jet (dark). View from $x = 0$ to $x/D_1 = 3$.

FIGURE 21. Angular cross-correlation function of velocity fluctuations for $\phi = 270°$.

FIGURE 22. Evolution of time shift τ_s as a function of phase angle ϕ.

reverse flow bubble rotates and oscillates at the same frequency. Indeed, the velocity fluctuation spectra show only one peak, interpreted as the pulsation frequency of the bubble. If the rotation phenomena were to happen at another frequency (different or a multiple of the oscillation frequency), this would show up in the spectrum analysis.

Ko & Lam's (1985) results confirm the existence of the azimuthal mode obtained from static pressure fluctuation measurements in an annular jet. They claimed that the wake flow creates so-called wake-induced vortices in the outer mixing region. These structures contain an azimuthal or helical mode which becomes more dominant compared with the axisymmetric mode as the gap width $(D_2 - D_1)/2$ gets smaller. The idea supported by these authors is based on the interaction between the inner and the outer mixing layers which has been, until now, not clear. The point of view developed below focuses rather on the interaction of the inner shear layer and the recirculating flow.

4.3. *Recirculation–induced oscillations*

This coaxial geometry presents the original property of sustaining a low-frequency pulsation once the recirculation regime is set up. Its frequency is unambiguously

distinguished from the Kelvin–Helmholtz preferred jet mode and is hardly sensitive to U_1 when $r_u \gg r_{uc}$. This wake frequency is essentially fixed by D_1 (the size of the recirculation bubble) and U_2 (the velocity scale which fixes the intensity of the backflow U_R) and is for the present geometry characterized by a Strouhal number of $St_b = fD_1/U_2 \approx 0.035$.

Following Villermaux (1994) and Villermaux *et al.* (1994), we provide here a 'minimal model' which contains all of the salient features of this phenomenon and which explains why and how the recirculation, existing in the vicinity of the shear layer produced by the outer jet, can sustain this low-frequency mode.

Consider a (spatially developing) shear layer experiencing a velocity difference ΔU. At a given location downstream from the beginning of its development, the shear layer has a thickness δ, steady in time. This steady state can be interpreted as a saturated state for the envelope of the disturbances $A(t)$ ($\sim \delta$) in such a way that $dA/dt = 0$. Imagine that an external perturbation modulates the thickness δ; the shear layer 'responds' to this perturbation with a growth rate r proportional to $\Delta U/\delta$ before returning to the stationary thickness δ. Now, if the perturbation comes from the shear layer itself, with a time delay corresponding to a transit time τ through a recirculation loop, the global dynamics results in a self-exited oscillatory behaviour via delayed interactions. This picture was modelled by an evolution equation for the (real) envelope $A(t)$ of the shear layer disturbances (whose frequency corresponds to the jet mode), which reads

$$\frac{d}{dt}A(t) = \left(r - \mu A^2(t-\tau)\right) A(t). \tag{6}$$

This equation, which is similar to the delayed logistic equation familiar from the population dynamics context and reduces to the Landau model for $r\tau < \pi/4$, displays nonlinear self-sustained oscillations whose period can be computed from the dynamical parameters r and τ (see e.g. Villermaux & Hopfinger 1994*b*). The parameter μ sets the amplitude of the oscillation only. The instantaneous effective growth rate $r_{eff} = r - \mu A^2(t-\tau)$ oscillates itself around zero when the delay τ is sufficiently larger than the characteristic time of the growth rate of the primary instability r^{-1} (i.e. $r\tau > \frac{1}{4}\pi$).

The estimation of r and τ for coaxial jets above the recirculation threshold (i.e. for $r_u > r_{uc}$) proceeds as follows. If δ is the thickness of the shear layer, bordering the recirculation zone, experiencing a velocity jump $\Delta U \sim U_2$, then $r \approx 0.2U_2/\delta$ (Monkewitz & Huerre 1982). δ might simply be estimated as the width of the annular gap, that is $(D_2 - D_1)/2$. The time delay τ is given by the size of the recirculation zone $\approx D_1$ divided by the return velocity $U_R \approx (0.3\text{–}0.4)\,U_2$, so that $\tau \approx D_1/0.4U_2$. Thus,

$$r\tau \approx \frac{D_1}{D_2 - D_1} \tag{7}$$

within a factor of order unity. In the present geometry and using the expression for the period of this slow oscillation (see e.g. Villermaux & Hopfinger 1994*b*, Villermaux *et al.* 1994), we find that $St_b = fD_1/U_2 \approx 0.034$, in agreement with the observed Strouhal number.

The above scenario for the origin of the oscillations essentially relies on two-dimensional arguments: the 'oscillator' is composed of a plane shear layer bordering a two-dimensional recirculation zone. However, the recirculation bubble of this coaxial

geometry bears an angular degree of freedom in planes parallel to the injector outlet. This is a common feature with other separated flows behind axisymmetric bluff bodies such as the disk or the sphere configuration. The actual problem thus consists of a periodic chain of several oscillators, coupled to each other via the recirculation, that is via the nonlinear delayed term of (6). Note that, since the delayed term is intended to represent the dynamical role of the recirculation, the coupling between the oscillators is, by construction, strongly non-local: two oscillators, diametrally opposed on each side of the recirculation bubble, are coupled to each other precisely because the recirculating motion occupies all of the available space of the bubble. This remark, made in a slightly different context, allowed the origin and the features of the low-frequency oscillations of the boundary layers close to the walls in closed convection boxes to be explained (Villermaux 1995*b*). It was found, consistently with the experimental observations, that the top and bottom boundary layers in the cell oscillate in phase opposition, as a consequence of the long-range, delayed coupling between the two sides of the convection cell (see also Ciliberto, Cioni & Laroche 1996).

The number of oscillators regularly distributed on the perimeter of the recirculating bubble is, according to our definition of what an 'oscillator' is in this type of problem, equal to the number of shear layer widths δ needed to cover the perimeter πD_1, i.e $N \approx \pi D_1/\delta$. Note that the continuous limit $N \to \infty$ has no reason to be justified in general, precisely because the structures embedded in the shear layer at these high Reynolds numbers have roughly an aspect ratio of order unity in the spanwise direction (spanwise width $\sim \delta$). We examine, for illustration here, a coarse grained version of this model consisting of four oscillators, symmetrically coupled. This number is close to the minimal number (three) to discuss the propagation of the phase of the oscillation in the azimuthal plane, and allows a direct comparison with the experimentally observed phase opposition between diametrically opposed oscillators. A continuous version of the model is of course also possible, with an appropriate weighting function for the amplitudes of the neigbouring oscillators in the evolution equation of a given oscillator.

The essential ingredient of the NLDS (nonlinear delayed saturation) model, aimed at describing recirculation-dominated flows, is the non-locality of the interactions in time. This also implies the non-locality of the interactions in space, these being mostly effective between facing oscillators (due to the axisymmetric nature of the recirculating mean flow), and, to a minor extent, between adjacent oscillators (which only contribute to a global bending of the shear layer of a reference oscillators, not to the modulation of its thickness). Let us consider the square of the amplitudes rescaled by r/μ (i.e. $a \equiv A^2/(r/\mu)$), and the dimensionless time $\theta = rt$. The evolution equation of oscillator n is thus

$$\frac{\mathrm{d}}{\mathrm{d}\theta}a_n(\theta) = 2a_n(\theta)\left\{1 - \left(a_n(\theta - \Theta) + c\left[a_{n+2}(\theta - \Theta)\right.\right.\right.$$
$$\left.\left.\left. + g\{a_{n+1}(\theta - \Theta) + a_{n+3}(\theta - \Theta)\}\right]\right)\right\} \tag{8}$$

with $\Theta = r\tau$, and c and g being respectively a coupling and a weighting parameter, both of them smaller than one. The only stationary solution of (8) with positive amplitudes is the synchronized mode $a_n = 1/(1 + c(1 + 2g)) = a_s$. The stability of this solution is investigated by imposing a small perturbation δa_n proportional to $\mathrm{e}^{s\theta + \mathrm{i}m2\pi(n-1)/N} + \mathrm{c.c}$ with $N = 4$. Linearizing (8) in δa_n and decomposing $s = s' + \mathrm{i}s''$,

one gets the dispersion relation in the form

$$\frac{s'}{-2\mathrm{e}^{-s\Theta}a_s} = \cos(s''\Theta)\left\{1 + c\left[\cos(m\pi) + g\{\cos(\tfrac{1}{2}m\pi) + \cos(\tfrac{3}{2}m\pi)\}\right]\right\}$$
$$+ c\sin(s''\Theta)\left[\sin(m\pi) + g\{\sin(\tfrac{1}{2}m\pi) + \sin(\tfrac{3}{2}m\pi)\}\right], \qquad (9a)$$

$$\frac{s''}{-2\mathrm{e}^{-s'\Theta}a_s} = -\sin(s''\Theta)\left\{1 + c\left[\cos(m\pi) + g\{\cos(\tfrac{1}{2}m\pi) + \cos(\tfrac{3}{2}m\pi)\}\right]\right\}$$
$$+ c\cos(s''\Theta)\left[\sin(m\pi) + g\{\sin(\tfrac{1}{2}m\pi) + \sin(\tfrac{3}{2}m\pi)\}\right]. \qquad (9b)$$

Figure 23 shows that the stationary solution first becomes unstable for $m = 0$ at $r\tau = \tfrac{1}{4}\pi$ (the same threshold value as for one single oscillator). For $r\tau > \tfrac{1}{4}\pi$, the oscillatory solution is, however, unstable in the synchronized mode ($m = 0$), while the rotation mode $m = 1$ remains stable up to $r\tau = \tfrac{1}{4}\pi(1 + c(1 + 2g))/(1 - c)$. The mode $m = 2$ has weaker stability compared to $m = 1$ and destabilizes earlier when $r\tau$ is increased; that is for $r\tau > \tfrac{1}{4}\pi(1 + c(1 + 2g))/(1 + c(1 - 2g))$ close to the oscillation threshold, the stable saturated limit cycle has thus the $m = 1$ symmetry.

We have emphasized that the oscillatory solution of the NLDS model is a consequence of the non-locality of the interactions in time. The phase opposition between facing oscillators leading to the $m = 1$ mode is, in turn, a consequence of the non-locality of the interactions in space, consistent with the picture of the flow underlying the NLDS formulation, that is the role played by the slow recirculating motion. For the case of two coupled oscillators (Villermaux 1995b), the stable oscillatory configuration in (8) is the one which maximizes the apparent growth rate of a_n, thus selecting the $m = 1$ mode. This result is, although interpreted differently, consistent with the linear stability analysis of mean velocity profiles reflecting similar flow configurations (Monkewitz 1988).

This situation has to be contrasted with other experimental situations which also exhibit vortex shedding with periodic boundary conditions, as in the wake of a torus studied in great details by Leweke & Provansal (1995) for which it is known that the symmetric $m = 0$ mode is preferentially selected. Ignoring the phase opposition of the shedding process at the scale of the rod forming the ring (very similar to the Bénard vortex shedding process), and assuming the oscillation associated with the shedding to be due to a single oscillator locally, these authors showed how a weak, synchronous diffusive coupling between neighbouring oscillators on the torus (Ginsburg–Landau model) accounts for the stability limits of the different modes, consistently with their observations. The fact that the $m = 0$ mode is preferred in that case is not surprising in view of our previous discussion since, by construction, the geometry of the torus does not allow for a long range coupling between the diametrically opposed recirculation zones downstream of the ring as it is the case for the disc, the sphere (Achenbach 1974; Berger *et al.* 1990), or the coaxial geometry above recirculation threshold.

5. Conclusions

In this paper, the near-field flow characteristics of high-velocity-ratio ($r_u > 1$) and high-Reynolds-number coaxial jets is presented. It is shown that the near-field flow structure for $r_u > 1$ is dominated by the annular jet and is strongly dependent on r_u which appears to be the main parameter. For moderate velocity ratios ($1 < r_u < 8$), the inner cone length varies as A/r_u, with the numerical constant $A \approx 5$ to 9, depending on both the diameter ratio β and the mean velocity profiles at the nozzle
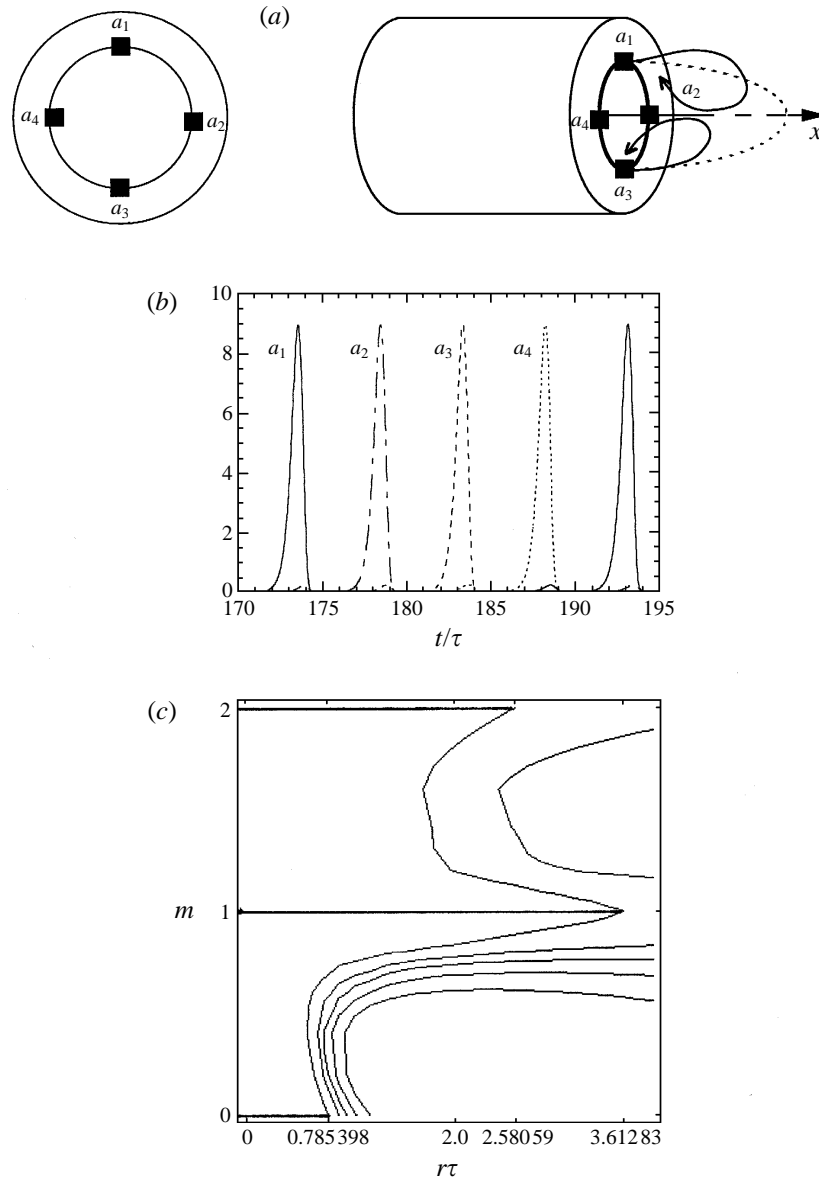
FIGURE 23. (*a*) Definition sketch of the azimuthal positions of the four oscillators of model (8) regularly spaced on the periphery of the recirculation bubble. (*b*) Time evolutions of the amplitudes of the oscillators a_1, a_2, a_3 and a_4 over a period of oscillation according to (8). The $m = 1$ mode is obvious. $r\tau = 1.6$, $c = 0.5$ and $g = 0.8$. (*c*) Diagram of stability of system (9) for $c = 0.5$ and $g = 0.8$. From left to right, the iso-contours correspond to instability growth rate $s'\tau = 0$, 0.1, 0.2, 0.3, 0.4 and 0.5, as computed from (9*a*) and (9*b*). The allowed modes correspond to the discrete values of $m = 0, 1$ and 2.

exits, specifically on the ratio $(U/\overline{U})$. A simple model based on mass conservation and an entrainment hypothesis explains the physical mechanisms governing the flow and leads to an expression for the inner cone length, in good agreement with the experimental result.

Above a critical velocity ratio r_{uc}, the inner potential cone is truncated by a reverse

flow and a wake-type regime is active. This new flow pattern is characterized by the existence of an unsteady recirculation bubble. The transition mechanism to a wake regime is explained by a simple model which predicts satisfactorily r_{uc}. The size of the recirculating bubble increases with r_u and reaches a maximum length for $r_u = \infty$, typically equal to one inner jet diameter D_1. The mean reverse flow velocity is proportional to U_2. Velocity and mean static pressure measurements confirm our reasoning concerning the two flow regimes and the transition to a recirculating flow.

The recirculation bubble oscillates with low frequency ($St_b = fD_1/U_2 = 0.035$) and with large amplitude. Velocity cross-correlations in the plane parallel to the jet outlets show that this oscillation is an azimuthal precession mode such that the rotation time of the phase of the oscillations is equal to the oscillation period. The origin of the low-frequency oscillations is explained by the NLDS model.

REFERENCES

ACHENBACH, E. 1974 Vortex shedding from spheres. *J. Fluid Mech.* **62**, 209–221.

AU, H. & KO, N. W. M. 1987 Coaxial jets of different mean velocity ratios. *J. Sound Vib.* **116**, 427–443.

BECKER, H. A. & MASSARO, T. A. 1968 Vortex evolution in a round jet. *J. Fluid Mech.* **31**, 435–448.

BERGER, E., SCHOLZ, D. & SCHUMM, M. 1990 Coherent vortex structures in the wake of a sphere and a circular disk at rest and under forced vibrations. *J. Fluid Structures* **4**, 231–257.

BROWAND, G. L. & LATIGO, A. 1979 On density effects and large scale structures in turbulent mixing layers. *J. Fluid Mech.* **64**, 775–815.

BROWN, G. L. & ROSHKO, A. 1974 On density effects and large scale structures in turbulent mixing layers. *J. Fluid Mech.* **64**, 775–815.

CHAMPAGNE, F. H. & WYGNANSKI, I. J. 1971 An experimental investigation of coaxial turbulent jets. *J. Heat Mass Transfer.* **4**, 1445–1464.

CHAN, W. T. & KO, N. W. M. 1978 Coherent structures in the outer mixing region of annular jets. *J. Fluid Mech.* **89**, 515–533.

CHIGIER, N. A. & BEER, J. M. 1964 The flow region near the nozzle in double concentric jets. *Trans. ASME* D: *J. Basic Engng* **86**, 794–804.

CILIBERTO, S., CIONI, S. & LAROCHE, C. 1996 Large scale flow properties of turbulent thermal convection. *Phys. Rev.* E **54**, 5901–5905.

CROW, S. C. & CHAMPAGNE, F. H. 1971 Orderly structure in jet turbulence. *J. Fluid Mech.* **48**, 547–91.

DAHM, W. J. A., CLIFFORD, E. F. & TRYGGVANSON, G. 1992 Vortex structure and dynamics in the near field of a coaxial jet. *J. Fluid Mech.* **241**, 371–402.

GLADNICK, P. G., ENOTIADIS, A. C., LARUE, J. C. & SAMUELSEN, G. S. 1990 Near-field characteristics of a turbulent coflowing jet. *AIAA J.* **28**, 1405–1414.

HILL, B. J. 1972 Measurement of local entrainment rate in the initial region of axisymmetric turbulent air jets. *J. Fluid Mech.* **51**, 773–779.

HINZE, J. O. 1959 *Turbulence.* McGraw-Hill.

HO, C.-M. & HUERRE, P. 1984 Perturbed free shear layers. *Ann. Rev. Fluid Mech.* **16**, 365–424.

HUSSAIN, A. K. M. F. & ZEDAN, M. F. 1978 Effects of the initial condition on the axisymmetric free shear layer: Effects of the initial momentum thickness. *Phys. Fluids* **21**, 1100–1112.

KO, N. W. M. & CHAN, W. T. 1978 Similarity in the initial region of annular jets: three configurations. *J. Fluid Mech.* **84**, 641–656.

KO, N. W. M. & CHAN, W. T. 1979 The inner region of annular jets. *J. Fluid Mech.* **93**, 549–584.

KO, N. W. M. & LAM, K. M. 1985 Flow structures of a basic annular jet. *AIAA J.* **23**, 1185–1190.

LAM, K. M. & KO, N. W. M. 1986 Investigation of flow structures of a basic annular jet. *AIAA J.* **24**, 1488–1493.

LANDAU, L. D. & LIFCHITZ, E.M. 1989 *Mécanique des Fluides*. Mir, Moscow.

LEFEBVRE, A. H. 1989 *Atomization and Sprays. Combustion, An international Series*. Taylor & Francis.

LEWEKE, T. & PROVANSAL, M. 1995 The flow behind rings: bluff body wakes without end effects. *J. Fluid Mech.* **288**, 265–310.

LIEPMANN, D. & GHARIB, M. 1994 The role of streamwise vorticity in the near-field entrainment of round jets. *J. Fluid Mech.* **245**, 643–668.

MILLER, D. R. & COMINGS, E. W. 1960 Force-momentum fields in a dual jet flow. *J. Fluid Mech.* **7**, 247–256.

MONKEWITZ, P. A. 1988 The absolute and convective nature of instability in two-dimensional wakes at low Reynolds numbers. *Phys. Fluids* **31**, 999–1006.

MONKEWITZ, P. A. & HUERRE, P. 1982 The influence of the velocity ratio on the spatial instability of mixing layers. *Phys. Fluids* **25**, 1137–1143.

REHAB, H., VILLERMAUX, E. & HOPFINGER, E. J. 1997 Geometrical effects on the near field flow structure of coaxial jets. *AIAA J.* (submitted).

SCHLICHTING, H. 1987 *Boundary Layer Theory*. McGraw-Hill.

STRYOWSKI, P. J. & NICCUM, D. L. 1991 The stability of countercurrent mixing layers in circular jets. *J. Fluid Mech.* **227**, 309–343.

VILLERMAUX, E. 1994 Pulsed dynamics of fountains. *Nature.* **371**, 24–25.

VILLERMAUX, E. 1995*a* Fast bimolecular reactions in high Reynolds number turbulence: Structure of the reactive interface and surface of reaction. In *Advances in Turbulence* (ed. R. Benzi), pp. 529–533. Kluwer.

VILLERMAUX, E. 1995*b* Memory-induced low frequency oscillations in closed convection boxes. *Phys. Rev. Letts.* **75**, 4618–4621.

VILLERMAUX, E. & DUROX, D. 1992 On the physics of jet diffusion flames. *Combust. Sci. Tech.* **84**, 279–294.

VILLERMAUX, E. & HOPFINGER, E. J. 1994*a* Periodically arranged co-flowing jets. *J. Fluid Mech.* **263**, 63–92.

VILLERMAUX, E. & HOPFINGER, E. J. 1994*b* Self-sustained oscillations of a confined jet: a case study for the non-linear delayed saturation model. *Physica* D **72**, 230–243.

VILLERMAUX, E., REHAB, H. & HOPFINGER, E. J. 1994 Breakup regimes and self-sustained pulsations in coaxial jets. *Meccanica* **29**, 393–401.